Photodetachment of He^- $1s2s2p\,^4P^o$ in the region of the $1s$ threshold

H. L. Zhou and S. T. Manson
Department of Physics and Astronomy, Georgia State University, Atlanta, Georgia 30303

L. Vo Ky*
Center for Theoretical Studies of Physical Systems, Clark-Atlanta University, Atlanta, Georgia 30314

A. Hibbert
Department of Applied Mathematics and Theoretical Physics, The Queen's University of Belfast, Belfast BT7 1NN, United Kingdom

N. Feautrier
DAMAP, UMR 8588 du CNRS, Observatoire de Paris, 92195 Meudon Cedex, France
(Received 5 December 2000; published 8 June 2001)

The photodetachment cross section of the $1s2s2p\,^4P^o$ metastable state of He^- in the region of the $1s$ threshold has been calculated using our enhanced *R*-matrix code with the asymptotic part upgraded to handle a negative-ion system. The results show a $1s$ photodetachment cross section with numerous structures, completely different from similar situations in atoms or positive ions. This is found to be due to the dominance of correlation of both initial *and* final states of the negative ion. Specifically, interchannel coupling and a newly identified multiconfiguration overlap effect are primarily responsible for the dramatic $1s$ photodetachment cross-section phenomenology. Comparison with a previous calculation has been made and, while there are some areas of excellent agreement, overall there are very serious discrepancies, as much as an order of magnitude.

DOI: 10.1103/PhysRevA.64.012714 PACS number(s): 32.80.Gc

I. INTRODUCTION

Negative atomic ions provide a great theoretical challenge because they are extremely sensitive to electron correlation effects. Studies of negative ions, therefore, are quite useful to help us to understand the general character of correlation effects in atomic systems. Over the past few years, the advent of appropriate lasers have engendered a number of experimental studies of negative-ion photodetachment for the outer shell [1]. But there are almost no experimental investigations into inner-shell photodetachment of negative ions, and none for $1s$ shells. On the theoretical side, several highly sophisticated computational techniques have been developed to deal with photoabsorption by atomic systems; included in these methods is the *R*-matrix methodology. This method has been extensively employed to study the photoionization of atoms and positive ions [2]. But it has not been much applied to photodetachment of negative ions. This has been due to the lack of an efficient outer-region asymptotic code. Because the neutral target electron effectively screens the ionic charge, there is no long-range Coulomb field. The outer electron moves in a potential which is strongly affected by polarization and correlation. The traditional *R*-matrix asymptotic code [2] is not reliable in such circumstances.

Recently the *R*-matrix's asymptotic code, modified to use the variable phase method (VPM) in the outer region, was applied to the photodetachment of C^- and Li^- [3]. More recently, the method was applied to the photodetachment cross section for the $1s2s2p\ ^4P^o$ metastable state of the negative helium ion at low energies [4]. It was found that the VPM code exhibited numerical difficulties when applied to the photodetachment of $1s2s2p\ ^4P^o$ He^- around the $1s$ threshold. Therefore we have modified the *R*-matrix asymptotic code using another variable phase method package [5], one which we believe corrects the difficulties for inner-shell photodetachment. To test our methodology, He^- $1s2s2p\ ^4P^o$ photodetachment was calculated from the detachment threshold, $1s2s\ ^3S$ of He to 4 eV, and we find very good agreement with earlier calculations and experiment for the outer shells [4,6–8]. We therefore focus on the higher-energy region where $1s$ electrons can be detached. The basic equations are the same as in [3,9]. However, we used an appropriate Gailitis expansion [10] for the solutions in the asymptotic region and thereby get stable solutions.

An important motivation for looking at inner shells of negative ions emerges from a recent theoretical study of the photodetachment of the $1s2s2p\ ^4P^o$ state of He^- from threshold to 100 eV undertaken using multiconfiguration Hartree-Fock (MCHF) wave functions for discrete states and a continuum configuration-interaction (CI) method for resonances [11,12]. Coupling between open channels was not, however, included. Nevertheless, a number of new and unexpected features of the cross section in the vicinity of the $1s$ threshold were uncovered. Most recently a detailed investigation of the photodetachment of He^- was performed by Xi and Fischer [7,13] and by Liu and Starace [6] for energies below the $He(n=5)$ threshold and in the $1s$ detachment. Reference [13] also showed new phenomena in the $1s$ threshold region. These investigations encouraged us to study the inner-shell photodetachment of He^- of $1s2s2p$

*Permanent address: DAMAP, UMR 8588 du CNRS, Observatoire de Paris, 92195 Meudon Cedex, France.

$^4P^o$ over a broad energy region to understand the phenomenology, to test the code convergence and stability of our new *R*-matrix asymptotic codes for negative ions, and to provide guidance for future experiments.

II. CALCULATIONAL DETAILS

A. Calculational method in outer region

In the *R*-matrix method [2], configuration space is divided into two regions: the inner region where exchange and short-range interactions are important, and the outer region where only long-range potentials have to be taken into account. The commonly used technique in the outer region is to solve the system of linear second-order differential equations directly by using an asymptotic expansion technique [2]. In the case of neutral atom targets, the previous asymptotic expansion technique may not be valid even for very large r in the near threshold region; moreover, when some channels are closed, but strongly coupled with open channels even away from threshold, direct inwards integration gives solutions which have very poor linear independence at the matching boundary. In order to solve this problem, a more powerful algorithm has been developed using the variable phase method and this theory has been described in detail elsewhere [5,9]. Basically, in the outer region $r>r_a$

$$\left(\frac{d^2}{dr^2}-\frac{l_i(l_i+1)}{r^2}+\frac{2Z}{r}+k_i^2\right)F_{ij}(r)=2\sum_{k=1}^{n}V_{ik}(r)F_{kj}(r), \tag{2.1}$$

where n is the number of coupled channels, and the direct potential V_{ij} is given by

$$V_{ij}(r)=\sum_{\lambda=1}a_{ij}^{\lambda}r^{-(\lambda+1)}. \tag{2.2}$$

The F_{ij} are the solutions representing the motion of continuum electron, and can be written in matrix form

$$\mathbf{F}=\mathbf{JA}-\mathbf{NB} \tag{2.3}$$

with the derivatives

$$\mathbf{F}'=\mathbf{J}'\mathbf{A}-\mathbf{N}'\mathbf{B}, \tag{2.4}$$

where **J** and **N** are appropriately normalized Bessel and Neumann functions, respectively. Equation (2.4) is equivalent to a supplementary condition

$$\mathbf{JA}'-\mathbf{NB}'=0 \tag{2.5}$$

with the **K** matrix is defined as

$$\mathbf{K}=\mathbf{BA}^{-1} \tag{2.6}$$

and its derivative

$$\mathbf{K}'=(\mathbf{B}'-\mathbf{KA}')\mathbf{A}^{-1}. \tag{2.7}$$

One can get the second derivative of **F** from Eq. (2.4) and then combine Eq. (2.1) to find $\mathbf{A}'$ and $\mathbf{B}'$. Finally, the derivative equation of the **K** matrix turns out to be [5]

$$\mathbf{K}'=-(\mathbf{J}-\mathbf{KN})\mathbf{V}(\mathbf{J}-\mathbf{NK}). \tag{2.8}$$

The K matrix is calculated starting at the *R*-matrix box boundary r_a, and integrating outwards to r_b where the Gailitis asymptotic expansion [5] is applicable. When the K matrix is obtained at r_b, A and B at r_b follow from Eqs. (2.3) and (2.6). We then integrate inward to r_a and get A and B at every point from r_b to r_a. Finally each wave function F_{ij} is obtained from Eq. (2.3). We choose a suitable Gailitis expansion in order to have reasonably small r_b, which also saves CPU time.

B. Target states of neutral helium

The process of the photodetachment of the $1s2s2p$ ($^4P^o$) state of He^- is

$$He^-(1s2s2p)(^4P^o)+h\nu\rightarrow He+e(^4S^e,^4P^e,^4D^e). \tag{2.9}$$

Since all final states of the $e+$ He system are quartets, all of the target states of He must therefore have triplet spin symmetry. Hence the number of states is fewer than we needed in our previous work on inner-shell photoionization of Li [14].

Previously, Spline-Galerkin and inverse iteration methods have been used to investigate the photodetachment cross section [7,13]. Multiconfiguration Hartree-Fock (MCHF) wave functions were calculated for the states $1snl\ ^3L$ ($n\leqslant 5, l\leqslant 3$) for a study of the cross section with photon energies up to 4 eV [7], while $1snl\ ^3L$ ($n\leqslant 3, l\leqslant 2$) plus $2snl$, $2pnl$ ($n\leqslant 3, l\leqslant 2$ and $4s$) were used to study the cross section in the region of the $1s$ detachment threshold [13]. There are some similarities between that method and the *R*-matrix calculation, including the need to define target states. In the present work, we have calculated configuration-interaction wave functions using the code CIV3 [15] for all the above target states. These wave functions are expressed in the form

$$\Phi_i(S_iL_i)=\sum_{j=1}^{M}a_{ij}\psi_j(\alpha_jS_iL_i), \tag{2.10}$$

where the M configuration state functions ψ_j are constructed from one-electron orbitals of the form

$$\frac{1}{r}P_{nl}(r)Y_l^{m_l}(\theta,\phi)\chi_{m_s}(\sigma) \tag{2.11}$$

with the angular momenta coupled according to α_j to form a total S_iL_i. The coefficients a_{ij} are the eigenvector components of the Hamiltonian matrix whose typical element is $\langle\psi_j|H_N|\psi_k\rangle$, where H_N is the N-electron target Hamiltonian. The corresponding eigenvalues E_i of any $S_iL_i\pi$ symmetry are the calculated target state energies, and satisfy the inequalities

TABLE I. Radial function parameters.

nl	C_{jnl}	I_{jnl}	ζ_{jnl}	nl	C_{jnl}	I_{jnl}	ζ_{jnl}
$1s$	1.00000	1	2.00000	$5p$	0.49308	2	0.43654
$2s$	0.25791	1	1.57891		−4.88007	3	0.20894
	−1.05773	2	0.59942		8.86096	4	0.20938
$3s$	0.13462	1	1.55417		−4.89010	5	0.19628
	−1.29676	2	0.43294	$6p$	1.41872	2	1.63103
	1.84539	3	0.38195		−0.88912	3	1.16132
$4s$	0.08509	1	1.53713		0.16570	4	0.43044
	−1.40629	2	0.35099		0.19528	5	0.18163
	2.91733	3	0.33406		−0.24694	6	0.25885
	−2.16177	4	0.26667	$7p$	3.41494	2	0.89299
$5s$	0.06082	1	1.52610		−4.99717	3	1.13495
	−1.87151	2	0.27410		1.69275	4	0.92477
	6.30854	3	0.26433		1.18282	5	0.18564
	−6.40915	4	0.26365		−15.87115	6	0.26035
	2.39312	5	0.20038		14.76137	7	0.30221
$6s$	5.36040	1	0.42671	$3d$	1.00000	3	0.33361
	−17.15148	2	0.99631	$4d$	1.97489	3	0.25531
	12.71993	3	1.53344		−2.48945	4	0.25000
	−1.40025	4	0.35705	$5d$	6.69420	3	0.16726
	0.92118	5	0.32335		−9.59266	4	0.20715
	−0.15111	6	0.23095		3.23947	5	0.20450
$7s$	10.60036	1	0.44579	$6d$	1.38052	3	1.73673
	−20.37883	2	0.99631		−0.57055	4	1.36247
	10.60975	3	1.54031		0.01198	5	0.47861
	−5.62664	4	0.31702		−0.00378	6	0.10230
	1.18401	5	0.27338	$7d$	0.53813	3	1.89934
	3.65364	6	0.38276		−1.29879	4	1.20571
	−0.64343	7	0.23594		0.60972	5	0.55757
$2p$	1.00000	2	0.54402		0.48954	6	0.21444
$3p$	0.69904	2	0.50834		−0.67118	7	0.31942
	−1.25395	3	0.31460	$4f$	1.00000	4	0.25000
$4p$	0.60200	2	0.46083	$5f$	2.21464	4	0.20602
	−2.59040	3	0.26131		−2.66780	5	0.19965
	2.71187	4	0.24364				

$$E_i \geqslant E_i^{\text{exact}}, \tag{2.12}$$

where we assume the eigenvalues are ordered: $E_1 < E_2 < \ldots$.

The inequalities (2.12) constitute variational principles from which to optimize the radial functions $P_{nl}(r)$ in Eq. (2.11). They apply equally to the ground and excited bound states as to doubly excited states of two electron ions [16]. Specifically, each radial function may be optimized on one of the E_i, potentially a different eigenvalue for each radial function.

The target states in these calculations are expressed in analytic form,

$$P_{nl}(r) = \sum_{j=1}^{k} C_{jnl} N_{jnl} r^{I_{jnl}} \exp(-\zeta_{jnl} r), \tag{2.13}$$

where N is a normalization factor

$$N_{jnl} = \left[\frac{(2\zeta_{jnl})^{2I_{jnl}+1}}{(2I_{jnl})!} \right]^{1/2}. \tag{2.14}$$

The value of k has been set equal to $n-l$, so that the coefficients C_{jnl} are uniquely determined by the orthonormality requirements

$$\int_0^\infty P_{nl}(r) P_{n'l}(r) dr = \delta_{nn'}. \tag{2.15}$$

All the target states that involve the $1s$ orbital are of the form $1snl$. For these, the $1s$ electron is almost unshielded from the nucleus by the other electron, so it is a good approximation to represent $1s$ by a purely hydrogenic function. The radial functions for the nl orbitals ($n \leqslant 5$) were then optimized on the energy of the corresponding $1snl\ ^3L$ states. The influence of electron correlation, which is a short-range effect, is felt most strongly in the lower-lying states.

TABLE II. Energies of target states in the CC expansion and their relative value to the He^- $1s2s2p\ ^4P^o$ initial state (1 Ry = 13.605 804 eV is used to convert Ry to eV).

Target	Energy [a] (a.u.)	Relative to He^- [a] (Ry)	(eV)	Energy [b] (a.u.)	Relative [b] (Ry)
$He(1s2s\ ^3S)$	−2.175117	0.005632	0.0766	−2.175202	0.005694
$He(1s2p\ ^3P^o)$	−2.132969	0.08993	1.2235	−2.133157	0.08978
$He(1s3s\ ^3S)$	−2.068656	0.21855	2.9736	−2.068683	0.21873
$He(1s3p\ ^3P^o)$	−2.058019	0.23983	3.2630	−2.058058	0.23998
$He(1s3d\ ^3D)$	−2.055604	0.24466	3.3288	−2.055636	0.24483
$He(2s2p\ ^3P^o)$	−0.758251	2.83936	38.6318	−0.760458	2.83518
$He(2p^2\ ^3P)$	−0.708737	2.93839	39.9791	−0.710492	2.93512
$He(2s3s\ ^3S)$	−0.600375	3.15511	42.9278	−0.602486	3.15113
$He(2s3p+2p3s\ ^3P^o)$	−0.582778	3.19031	43.4067	−0.584580	3.18694
$He(2p3p\ ^3D)$	−0.580561	3.19474	43.4670	−0.583669	3.18878
$He(2s3p-2p3s\ ^3P^o)$	−0.576099	3.20367	43.5885	−0.578990	3.19812
$He(2p3p\ ^3P)$	−0.565061	3.22574	43.8888	−0.567729	3.22064
$He(2p3d\ ^3F)$	−0.560656	3.23455	44.0087	−0.565928	3.22424
$He(2p3p\ ^3S)$	−0.557148	3.24157	44.1042	−0.558841	3.23842
$He(2s3d\ ^3D)$	−0.556172	3.24352	44.1307	−0.560198	3.23570
$He(2s4s\ ^3S)$	−0.545869	3.26413	44.4110	−0.548217	3.25967
$He(2p3d\ ^3P^o)$	−0.545521	3.26482	44.4205	−0.548813	3.25847

[a]Present work.
[b]Reference [13].

$6s,6p,6d$ functions were optimized on the $1s2s\ ^3S$ state, to take this effect into account. This set of functions is still not completely adequate for the representation of the doubly excited states, so the functions of $7s,7p,7d$ were optimized on the eigenvalue corresponding to the $2s2p\ ^3P^o$ state. The final parameters of all the radial functions are displayed in Table I.

In order to compare our results with the recent calculation [13] in the $1s$ detachment region, we used the same 17 target states as [13] in the *R*-matrix close-coupling expansion. Table II shows our calculated energies and compares them with the MCHF results [13], which used a somewhat more extensive set of orbitals than we have. We were concerned to limit the orbital set to ensure that the *R*-matrix calculation did not become too large. Nevertheless, the two sets of calculated energies agree well, though it would appear that our energies for the $2s3d$ and $2p3d$ are slightly too high.

Oscillator strengths for transitions between these states of neutral He are shown in Table III as a test of the quality of the discrete wave functions used in this calculation. Except for the weak lines, the agreement between length and velocity forms is very good: mostly within 2%. A comparison of our calculations and those of previous authors is shown in Table IV. The calculations of [17] were undertaken with an extensive use of interelectronic coordinates and are widely regarded as being the most accurate available. The calculations [18] undertaken as part of the Opacity Project agree closely with those of Ref. [17], though unlike [17], they also include $p \rightarrow d$ transitions. The much earlier configuration-interaction calculations of [19] were less extensive than any of the more recent calculations and for some of the transitions display a slightly wider variation between length and velocity forms. Our own calculations agree well with the Opacity Project calculations, and we note that our velocity form appears to be slightly more accurate. For this two-electron system that is understandable, since the radial functions are determined variationally and the potential-energy operator and the velocity form of the oscillator strength emphasizes essentially the same region of space. On the basis of the agreement of the discrete oscillator strengths, we are therefore confident that our wave functions provide a good representation of the target states for the *R*-matrix calculation.

C. (Target He+e) calculation

The initial $1s2s2p\ ^4P^o$ state of He^- and the final continuum states are calculated using the same basis functions with the additional of continuum basis functions for each orbital angular momentum $N^{cont}=60$, and angular momenta of scattered electron $l \leqslant 4$. Because target orbitals up to $n=7$, $l=3$ are included, an *R*-matrix radius $a=83a_0$ is chosen to ensure that the orbital functions approach zero at the boundary. We allowed a maximum of three electrons in p and d orbitals, and two electrons in f orbitals for the $N+1$ electron system. In the present work, we include exactly the same 17 states as Ref. [13] in the CC expansion, and also exactly the same open and closed channels as Ref. [13]. Using these states and channels in the *R*-matrix calculation, the electron affinity of the $1s2s\ ^3S$ He state is 0.005 631 91 Ry, 76.62 meV, which gives a bound-state energy of −2.177 932 8 a.u. for the $1s2s2p\ ^4P^o$ of the He^- initial

TABLE III. Oscillator strengths f and transition probabilities $A(s^{-1})$ in length and velocity formulations. Numbers in brackets denote powers of 10.

States						
Lower	Upper	λ(Å)	f_l	f_v	A_l	A_v
$1s2s\ ^3S$	$1s2p\ ^3P^o$	10807.55	0.5414	0.5404	1.030[7]	1.028[7]
	$1s3p\ ^3P^o$	3889.97	0.0635	0.0640	9.328[6]	9.403[6]
	$1s4p\ ^3P^o$	3189.33	0.0250	0.0256	5.470[6]	5.594[6]
	$1s5p\ ^3P^o$	2946.57	0.0108	0.0119	2.771[6]	3.051[6]
	$2s2p\ ^3P^o$	321.58	0.2483	0.2501	5.339[9]	5.378[9]
	$2s3p\ ^3P^o$	286.14	0.0040	0.0038	1.076[8]	1.033[8]
	$2p3s\ ^3P^o$	284.95	0.0546	0.0550	1.496[9]	1.505[9]
	$2p3d\ ^3P^o$	279.60	0.0007	0.0007	1.998[7]	2.093[7]
$1s2p\ ^3P^o$	$1s3s\ ^3S$	7082.59	0.0699	0.0693	2.788[7]	2.765[7]
	$1s4s\ ^3S$	4721.72	0.0108	0.0105	9.680[6]	9.407[6]
	$1s5s\ ^3S$	4127.50	0.0040	0.0038	4.744[6]	4.419[6]
	$2s3s\ ^3S$	297.30	0.0083	0.0082	1.879[9]	1.859[9]
	$2p3p\ ^3S$	289.14	0.0103	0.0103	2.468[9]	2.467[9]
	$2s4s\ ^3S$	287.09	0.0004	0.0004	1.009[8]	9.555[7]
	$2p^2\ ^3P$	319.92	0.1763	0.1780	1.149[10]	1.160[10]
	$2p3p\ ^3P$	290.60	0.0009	0.0009	7.409[7]	6.692[7]
	$1s3d\ ^3D$	5887.71	0.6119	0.6092	7.061[7]	7.029[7]
	$1s4d\ ^3D$	4479.04	0.1241	0.1221	2.474[7]	2.435[7]
	$1s5d\ ^3D$	4032.51	0.0492	0.0463	1.211[7]	1.139[7]
	$2p3p\ ^3D$	293.50	0.0816	0.0833	3.790[9]	3.869[9]
	$2s3d\ ^3D$	288.96	0.0171	0.0189	8.221[8]	9.080[8]
$1s3s\ ^3S$	$1s3p\ ^3P^o$	42826.41	0.8954	0.8844	1.085[6]	1.072[6]
	$1s4p\ ^3P^o$	12527.97	0.0480	0.0502	6.790[5]	7.113[5]
	$1s5p\ ^3P^o$	9464.98	0.0191	0.0223	4.725[5]	5.518[5]
	$2s2p\ ^3P^o$	347.70	0.0069	0.0045	1.263[8]	8.201[7]
	$2s3p\ ^3P^o$	306.64	0.1435	0.1414	3.394[9]	3.342[9]
	$2p3s\ ^3P^o$	305.27	0.1936	0.1955	4.619[9]	4.666[9]
	$2p3d\ ^3P^o$	299.14	0.0202	0.0203	5.017[8]	5.039[8]
$1s3p\ ^3P^o$	$1s4s\ ^3S$	21166.47	0.1457	0.1448	6.505[6]	6.462[6]
	$1s5s\ ^3S$	12864.39	0.0225	0.0224	2.717[6]	2.710[6]
	$2s3s\ ^3S$	312.58	0.0050	0.0055	1.023[9]	1.118[9]
	$2p3p\ ^3S$	303.58	0.0189	0.0196	4.103[9]	4.257[9]
	$2s4s\ ^3S$	301.31	0.0081	0.0075	1.777[9]	1.662[9]
	$2p^2\ ^3P$	337.69	0.0095	0.0097	5.575[8]	5.646[8]
	$2p3p\ ^3P$	305.19	0.1308	0.1330	9.366[9]	9.526[9]
	$1s3d\ ^3D$	188554.13	0.1110	0.1131	1.249[4]	1.272[4]
	$1s4d\ ^3D$	17030.14	0.4783	0.4775	6.597[6]	6.585[6]
	$1s5d\ ^3D$	11984.48	0.1226	0.1235	3.413[6]	3.439[6]
	$2p3p\ ^3D$	308.39	0.0832	0.0822	3.502[9]	3.461[9]
	$2s3d\ ^3D$	303.38	0.0435	0.0387	1.892[9]	1.684[9]
$1s3d\ ^3D$	$1s4p\ ^3P^o$	19543.57	0.0220	0.0221	6.392[5]	6.434[5]
	$1s5p\ ^3P^o$	12987.18	0.0039	0.0040	2.589[5]	2.618[5]
	$2s2p\ ^3P^o$	351.20	0.0000	0.0001	1.887[6]	1.176[7]
	$2s3p\ ^3P^o$	309.36	0.0055	0.0050	6.325[8]	5.832[8]
	$2p3s\ ^3P^o$	307.96	0.0146	0.0139	1.707[9]	1.633[9]
	$2p3d\ ^3P^o$	301.73	0.0538	0.0530	6.571[9]	6.468[9]
	$1s4f\ ^3F^o$	18705.55	1.0155	1.0152	1.382[7]	1.382[7]

TABLE III. (*Continued*).

States						
Lower	Upper	λ(Å)	f_l	f_v	A_l	A_v
	$1s5f\ ^3F^o$	12794.29	0.1567	0.1567	4.559[6]	4.558[6]
	$2p3d\ ^3F^o$	304.78	0.1619	0.1668	8.302[9]	8.553[9]
$1s4s\ ^3S$	$1s4p\ ^3P^o$	108381.25	1.2224	1.2106	2.313[5]	2.290[5]
	$1s5p\ ^3P^o$	28524.26	0.0400	0.0421	1.092[5]	1.150[5]
	$2s2p\ ^3P^o$	356.45	0.0044	0.0009	7.685[7]	1.626[7]
	$2s3p\ ^3P^o$	313.43	0.0059	0.0047	1.329[8]	1.055[8]
	$2p3s\ ^3P^o$	311.99	0.0040	0.0040	9.095[7]	9.139[7]
	$2p3d\ ^3P^o$	305.59	0.0026	0.0027	6.162[7]	6.384[7]
$1s4p\ ^3P^o$	$1s5s\ ^3S$	47030.82	0.2224	0.2227	2.011[6]	2.014[6]
	$2s3s\ ^3S$	318.20	0.0004	0.0007	7.646[7]	1.386[8]
	$2p3p\ ^3S$	308.87	0.0002	0.0003	3.427[7]	5.800[7]
	$2s4s\ ^3S$	306.53	0.0043	0.0055	9.166[8]	1.164[9]
	$2p^2\ ^3P$	344.25	0.0026	0.0027	1.472[8]	1.494[8]
	$2p3p\ ^3P$	310.54	0.0044	0.0046	3.066[8]	3.194[8]
	$1s4d\ ^3D$	444802.63	0.1993	0.1992	4.029[3]	4.027[3]
	$1s5d\ ^3D$	37078.35	0.4316	0.4379	1.256[6]	1.274[6]
	$2p3p\ ^3D$	313.85	0.0072	0.0064	2.911[8]	2.608[8]
	$2s3d\ ^3D$	308.67	0.0013	0.0002	5.643[7]	9.907[6]
$1s4d\ ^3D$	$1s5p\ ^3P^o$	42403.41	0.0512	0.0509	3.165[5]	3.147[5]
	$2s2p\ ^3P^o$	357.92	0.0003	0.0000	2.145[7]	3.939[6]
	$2s3p\ ^3P^o$	314.56	0.0003	0.0001	3.507[7]	1.537[7]
	$2p3s\ ^3P^o$	313.11	0.0008	0.0007	9.269[7]	8.218[7]
	$2p3d\ ^3P^o$	306.67	0.0001	0.0001	8.685[6]	1.369[7]
	$1s5f\ ^3F^o$	40414.00	0.8865	0.8865	2.584[6]	2.585[6]
	$2p3d\ ^3F^o$	309.82	0.0022	0.0031	1.100[8]	1.525[8]
$1s4f\ ^3F^o$	$1s5d\ ^3D$	40522.61	0.0090	0.0090	5.091[4]	5.108[4]
	$2p3p\ ^3D$	314.08	0.0001	0.0001	1.276[7]	1.307[7]
	$2s3d\ ^3D$	308.89	0.0049	0.0045	4.837[8]	4.378[8]
$1s5s\ ^3S$	$1s5p\ ^3P^o$	218888.44	1.5645	1.5374	7.256[4]	7.131[4]
	$2s2p\ ^3P^o$	360.37	0.0060	0.0003	1.024[8]	6.071[6]
	$2s3p\ ^3P^o$	316.45	0.0024	0.0013	5.311[7]	2.800[7]
	$2p3s\ ^3P^o$	314.99	0.0010	0.0010	2.344[7]	2.314[7]
	$2p3d\ ^3P^o$	308.47	0.0002	0.0003	5.534[6]	6.346[6]
$1s5p\ ^3P^o$	$2s3s\ ^3S$	320.83	0.0000	0.0002	7.588[6]	4.258[7]
	$2p3p\ ^3S$	311.36	0.0000	0.0001	1.390[6]	1.447[7]
	$2s4s\ ^3S$	308.98	0.0000	0.0008	1.092[6]	1.616[8]
	$2p^2\ ^3P$	347.34	0.0011	0.0011	5.913[7]	6.015[7]
	$2p3p\ ^3P$	313.05	0.0012	0.0013	8.341[7]	8.819[7]
	$1s5d\ ^3D$	878191.31	0.2802	0.2534	1.453[3]	1.314[3]
	$2p3p\ ^3D$	316.42	0.0027	0.0018	1.073[8]	7.312[7]
	$2s3d\ ^3D$	311.15	0.0023	0.0001	9.378[7]	2.514[6]
$1s5d\ ^3D$	$2s2p\ ^3P^o$	361.11	0.0036	0.0000	3.085[8]	1.636[6]
	$2s3p\ ^3P^o$	317.02	0.0004	0.0000	4.226[7]	2.303[6]
	$2p3s\ ^3P^o$	315.55	0.0002	0.0002	2.301[7]	2.082[7]

TABLE III. (*Continued*).

States						
Lower	Upper	λ(Å)	f_l	f_v	A_l	A_v
	$2p3d\ ^3P^o$	309.01	0.0000	0.0000	1.834[4]	8.107[5]
	$2p3d\ ^3F^o$	312.22	0.0001	0.0008	6.538[6]	3.956[7]
$1s5f\ ^3F^o$	$2p3p\ ^3D$	316.54	0.0000	0.0000	2.858[6]	4.596[6]
$2s2p\ ^3P^o$	$2s3s\ ^3S$	2885.17	0.0606	0.0617	1.455[8]	1.483[8]
	$2p3p\ ^3S$	2264.96	0.0060	0.0061	2.325[7]	2.367[7]
	$2s4s\ ^3S$	2144.66	0.0088	0.0083	3.824[7]	3.619[7]
	$2p^2\ ^3P$	9199.57	0.1820	0.1908	1.434[7]	1.503[7]
	$2p3p\ ^3P$	2357.75	0.0231	0.0242	2.766[7]	2.907[7]
	$2p3p\ ^3D$	2563.43	0.3581	0.3446	2.180[8]	2.097[8]
	$2s3d\ ^3D$	2254.03	0.1023	0.0860	8.054[7]	6.773[7]
$2p^2\ ^3P$	$2s3p\ ^3P^o$	3616.27	0.0019	0.0020	9.423[5]	1.041[6]
	$2p3s\ ^3P^o$	3434.17	0.1275	0.1196	7.209[7]	6.761[7]
	$2p3d\ ^3P^o$	2790.77	0.0870	0.0811	7.451[7]	6.939[7]
$2s3s\ ^3S$	$2s3p\ ^3P^o$	25885.26	0.4679	0.4077	1.552[6]	1.352[6]
	$2p3s\ ^3P^o$	18763.73	0.2498	0.2736	1.577[6]	1.727[6]
	$2p3d\ ^3P^o$	8304.05	0.0029	0.0018	9.409[4]	5.839[4]
$2s3p\ ^3P^o$	$2p3p\ ^3S$	17772.53	0.0005	0.0015	3.128[4]	9.682[4]
	$2s4s\ ^3S$	12341.34	0.0906	0.0882	1.189[7]	1.159[7]
	$2p3p\ ^3P$	25710.84	0.1427	0.1540	1.439[6]	1.553[6]
	$2p3p\ ^3D$	205484.14	0.0348	0.0214	3.299[3]	2.022[3]
	$2s3d\ ^3D$	17120.73	0.1951	0.1672	2.662[6]	2.281[6]
$2p3p\ ^3D$	$2p3s\ ^3P^o$	102085.37	0.0246	0.0074	2.622[4]	7.849[3]
	$2p3d\ ^3P^o$	12999.78	0.0053	0.0085	3.496[5]	5.601[5]
	$2p3d\ ^3F^o$	22884.35	0.3539	0.2159	3.218[6]	1.963[6]
$2p3s\ ^3P^o$	$2p3p\ ^3S$	24035.96	0.1114	0.1121	3.857[6]	3.881[6]
	$2s4s\ ^3S$	15067.92	0.0003	0.0002	2.679[4]	1.758[4]
	$2p3p\ ^3P$	41268.06	0.2108	0.1557	8.252[5]	6.093[5]
	$2s3d\ ^3D$	22859.02	0.4455	0.3028	3.410[6]	2.318[6]
$2p3p\ ^3P$	$2p3d\ ^3P^o$	23311.77	0.0850	0.0775	1.043[6]	9.504[5]
$2p3p\ ^3S$	$2p3d\ ^3P^o$	39178.38	1.0408	0.9600	1.507[6]	1.390[6]
$2s3d\ ^3D$	$2p3d\ ^3P^o$	42767.59	0.1052	0.0355	6.390[5]	2.158[5]

state. This is about 0.000 14 a.u. (3.8 meV) higher than the most accurate result [20]. Since the initial state is He^- $1s2s2p\ ^4P^o$ the final continuum states, by dipole selection rules, must be $^4S^e$, $^4P^e$, or $^4D^e$.

III. RESULTS AND DISCUSSION

To begin with, we examine the energy region just below the opening of the $1s$ detachment threshold. Since the $2s$ and $2p$ electrons are so weakly bound, and photoabsorption cross sections fall off roughly on the scale of the binding energy, the continuum cross sections of all channels arising from the outer electrons are quite small here, for energies well above their thresholds. However, the $1s \rightarrow 2p$ transition, which leads to the $2s2p^2\ ^4P^e$ Feshbach resonance, is significant; the $^4P^e$ cross section in this region is shown in Fig. 1. As it was discussed in Ref. [12], because the $2s$-$2p$ attractive exchange interaction is quite large, this makes the $2s2p^2\ ^4P^e$ discrete state lie below the $1s$ threshold. This contrasts with the $1s2p^2\ ^4P^e$ shape resonance, where the exchange in in-

TABLE IV. Comparison of oscillator strengths f in length and velocity form, with other calculations.

States		This work		Ref. [19]		Ref. [18]	Ref. [17]
Lower	Upper	f_l	f_v	f_l	f_v	f_l	f_l
$1s2s\ ^3S$	$1s2p\ ^3P^o$	0.5414	0.5404	0.540	0.549	0.5397	0.5391
	$1s3p\ ^3P^o$	0.0635	0.0640	0.0644	0.0668	0.0641	0.0645
	$1s4p\ ^3P^o$	0.0250	0.0256	0.0259	0.0271	0.0257	0.0258
	$1s5p\ ^3P^o$	0.0108	0.0119	0.0125	0.0132	0.0125	0.0125
$1s2p\ ^3P^o$	$1s3s\ ^3S$	0.0699	0.0693	0.0696	0.0685	0.0697	0.0695
	$1s4s\ ^3S$	0.0108	0.0105	0.0106	0.0104	0.0106	0.0106
	$1s5s\ ^3S$	0.0040	0.0038	0.0038	0.0037	0.0038	0.0038
	$1s3d\ ^3D$	0.6119	0.6092	0.6105	0.6269	0.611	
	$1s4d\ ^3D$	0.1241	0.1221	0.1232	0.1275	0.123	
	$1s5d\ ^3D$	0.0492	0.0463	0.0472	0.0490	0.047	
$1s3s\ ^3S$	$1s3p\ ^3P^o$	0.8954	0.8844	0.8922	0.9110	0.8927	0.8909
	$1s4p\ ^3P^o$	0.0480	0.0502	0.0499	0.0491	0.0497	0.0501
	$1s5p\ ^3P^o$	0.0191	0.0223	0.0228	0.0226	0.0228	0.023
$1s3p\ ^3P^o$	$1s4s\ ^3S$	0.1457	0.1448	0.1454	0.1461	0.1456	0.1452
	$1s5s\ ^3S$	0.0225	0.0224	0.0231	0.0226	0.0226	0.0227
	$1s3d\ ^3D$	0.1110	0.1131	0.1130	0.1216	0.111	
	$1s4d\ ^3D$	0.4783	0.4775	0.4766	0.4790	0.479	
	$1s5d\ ^3D$	0.1226	0.1235	0.1245	0.1254	0.124	
$1s3d\ ^3D$	$1s4p\ ^3P^o$	0.0220	0.0221	0.0223	0.0227	0.0221	
	$1s5p\ ^3P^o$	0.0039	0.0040	0.0042	0.0041	0.0041	
$1s4s\ ^3S$	$1s4p\ ^3P^o$	1.2224	1.2106	1.2164	1.2305	1.2173	1.2153
	$1s5p\ ^3P^o$	0.0400	0.0421	0.0439	0.0430	0.0438	0.044
$1s4p\ ^3P^o$	$1s5s\ ^3S$	0.2224	0.2227	0.2202	02247	0.2232	0.223
	$1s4d\ ^3D$	0.1993	0.1992	0.2023	0.2119	0.199	
	$1s5d\ ^3D$	0.4316	0.4379	0.4374	0.4363	0.440	
$1s4d\ ^3D$	$1s5p\ ^3P^o$	0.0512	0.0509	0.0531	0.0546	0.053	
$1s5s\ ^3S$	$1s5p\ ^3P^o$	1.5645	1.5374	1.5359	1.5383	1.5337	1.53
$1s5p\ ^3P^o$	$1s5d\ ^3D$	0.2802	0.2534	0.2815	0.2884	0.278	

teraction is weak due to the fact that $1s$ and $2p$ occupy rather different regions of space, which lies *above* the $1s2p\ ^3P$ threshold; a shape resonance [8]. Our results for the resonance position and width are 37.703 eV and 9.736 meV, respectively, in good agreement with Ref. [13] which reported the position and width as 37.669 eV and 9.850 meV, respectively. The results in length form and in velocity form differ less than 1% in our calculation; thus only the length form is shown in Fig. 1. Except for the 34-meV energy shift in position, the resonance shape and strength are nearly identical to the results of Ref. [13]. That means that the two calculations, employing rather different methods, treat the coupling between $1snlkl'$ channels and the $2s2p^2\ ^4P^e$ state to the same extent. An earlier calculation [12] did not take interchannel interaction among open channels into account, but considered only the main coupling of $1s2pkp\ ^4P$ and $2s2p^2\ ^4P$; nevertheless, the position and width reported for the $2s2p^2\ ^4P$ resonance was 37.683 eV and 9.22 meV, respectively, in good agreement with the present multichannel calculation. This suggests that the main interaction is the coupling between $1s2pkp\ ^4P$ and $2s2p^2\ ^4P$.

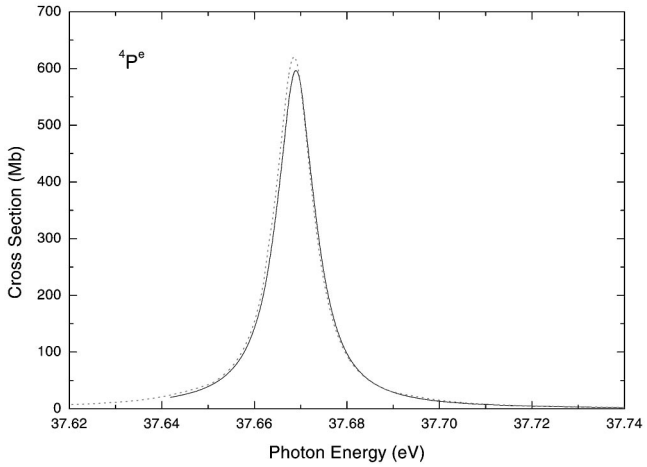

FIG. 1. $^4P^e$ photodetachment cross section of the $1s2s2p\ ^4P^o$ state of He^- showing the $2s2p^2\ ^4P^e$ resonance below the $1s$ threshold. The solid curve shows our present length results (curve shifted by 34 meV); the dotted line shows the calculated results from Ref. [13].

A. $^4P^e$ photodetachment cross section above the $1s$ threshold

The photodetachment cross section for the ^4P final state from just above the $1s$ threshold to 44 eV is shown in Fig. 2. At the $1s$ threshold, the cross section for outer-shell photodetachment ($1s2pkp$, $1s3pkp$, and $1s3dkd$ $^4P^e$ in this case) is only about 0.03 Mb. Above the opening of the $(2s2p\ ^3P)kp\ ^4P^e$ channel, the cross section increases to 6.8 Mb, just above the $1s$ detachment threshold. We emphasize that this is a *nonresonant* $1s2s2p\ ^4P^o \rightarrow (2s2p\ ^3P)kp\ ^4P^e$ cross section; photodetachment cross sections for each open channel are always zero at the channel threshold. This behavior is similar to the results of Ref. [13]. But around 40 eV, our results differ dramatically from Ref. [13]. The $(2p^2\ ^3P)ks$ and $(2p^2\ ^3P)kd$ channels open at 39.98 eV. Again, the cross section increases just above the $(2p^2\ ^3P)$ threshold. Reference [13] found two peaks and identified the sharp peak at 40.02 eV as due to $(2p^2\ ^3P)ks$ and the small peak at 40.3 eV from $(2p^2\ ^3P)kd$; our results, on the other hand, show only one wide peak, coming primarily from $(2p^2\ ^3P)ks$ at 40.14 eV. In order to investigate this discrepancy, we calculated the cross section using a very fine energy grid (0.00001 Ry) around 40 eV and the results are shown in Fig. 3. The main contribution is from the $(2p^2\ ^3P)ks$ channel, which is $1s$ detachment plus excitation. The $(2p^2\ ^3P)kd$ cross section is about a factor of 30 smaller than the ks channel. This is in substantial agreement with simpler MCHF results [11,12] which implies that interchannel coupling is relatively unimportant here. The implication is then that the transitions to the $(2p^2\ ^3P)$ channels come about through initial-state configuration interaction. The kd final state can be reached primarily from the $(2p^2\ ^3P)np\ ^4P^o$ configurations mixed into the initial state, but the coefficients are very small. The ks final state (a ''shake-off'' state) can be reached via $1sks2p$ and $2sks2p$ mixings in the initial state, whose CI coefficients are larger. The consistency of the present results with the earlier MCHF cross sections argues for their correctness. We, therefore, have no explanation for the discrepancy between our results and those of Ref. [13], which is so apparent in Fig. 2.

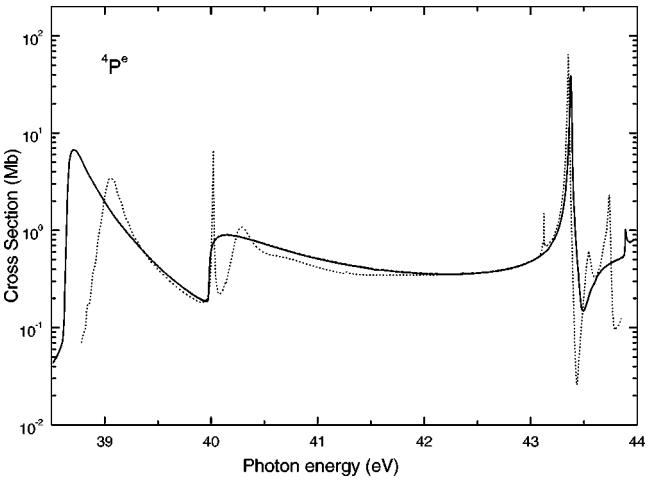

FIG. 2. $^4P^e$ photodetachment cross section of the $1s2s2p\ ^4P^o$ state of He^- from the $1s$ threshold to 44 eV. Present results: solid line, length form; dashed line, velocity form (results in length from and in velocity form are superimposed); the dotted line shows the result of Ref. [13].

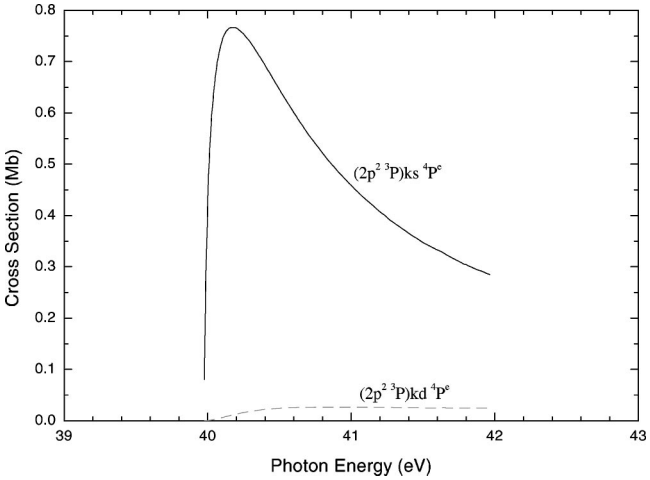

FIG. 3. Partial $^4P^e$ photodetachment cross section to $(2p^2\ ^3P)ks\ ^4P^e$, solid line; $(2p^2\ ^3P)kd\ ^4P^e$, dashed line. The dominant cross section of $(2p^2\ ^3P)ks\ ^4P^e$ is about 30 times larger than that of $(2p^2\ ^3P)kd\ ^4P^e$.

In order to investigate the resonance and threshold behavior in more detail, the $^4P^e$ partial cross sections leaving the target in specific states was studied for photon energies from 38.5 to 44 eV. Figure 4 shows the $^4P^e$ partial cross sections $\sigma(2s2p\ ^3P)$ and $\sigma(2p^2\ ^3P)$ in the vicinity of the $2p^2\ ^3P$ threshold, up to 43 eV. As described above, $\sigma(2p^2\ ^3P)$ like all photodetachment cross sections increases from zero at threshold. Due to the interchannel coupling with the much larger cross section of the $2p^2$ channel, $\sigma(2s2p\ ^3P)$ has a slight bump just at threshold. This interchannel coupling also results in the induced minimum in $\sigma(2s2p\ ^3P)$ because $\sigma(2p^2\ ^3P)$ is so dominant in that energy region. In Fig. 5 the results for the $^4P^e$ partial cross sections $\sigma(2s2p\ ^3P)$, $\sigma(2p^2\ ^3P)$, and $\sigma(23sp+\ ^3P)$ from 43 to 44 eV are shown.

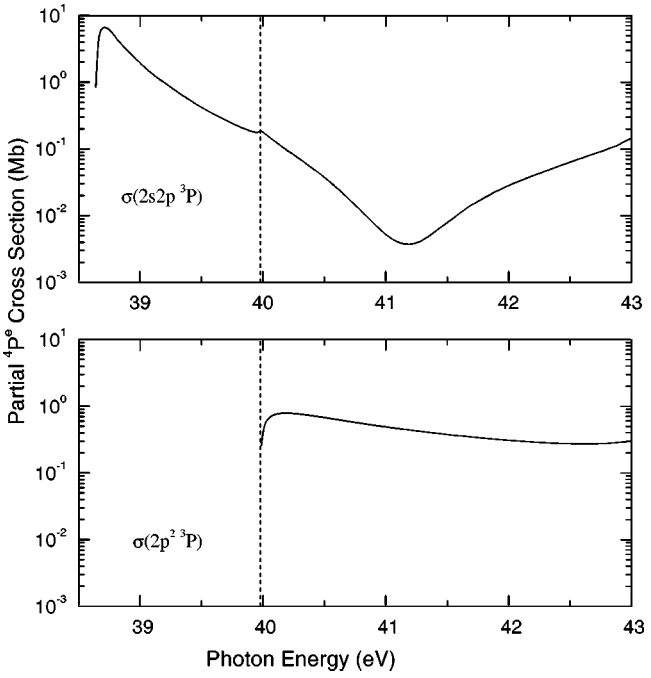

FIG. 4. Partial $^4P^e$ photodetachment cross sections leading to $2s2p\ ^3P$ and $2p^2\ ^3P$ states of neutral He. The vertical dashed line represents the He $2p^2\ ^3P$ threshold.

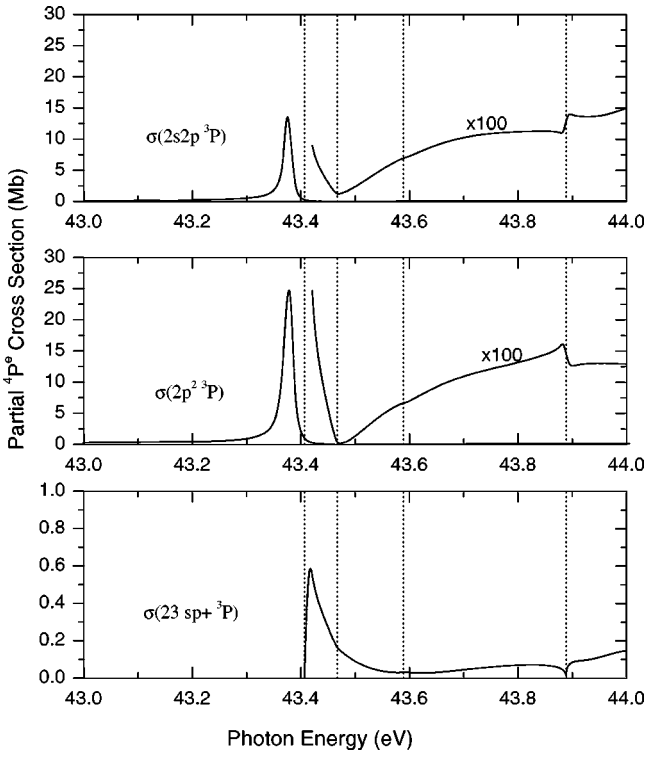

FIG. 5. Partial $^4P^e$ photodetachment cross sections leading to $2s2p\ ^3P$, $2p^2\ ^3P$, and $23sp+\ ^3P$ states of neutral He. The vertical dashed lines represent the He $23sp+\ ^3P$, $2p3p\ ^3D$, $23sp-\ ^3P$, and $2p3p\ ^3P$ thresholds, respectively.

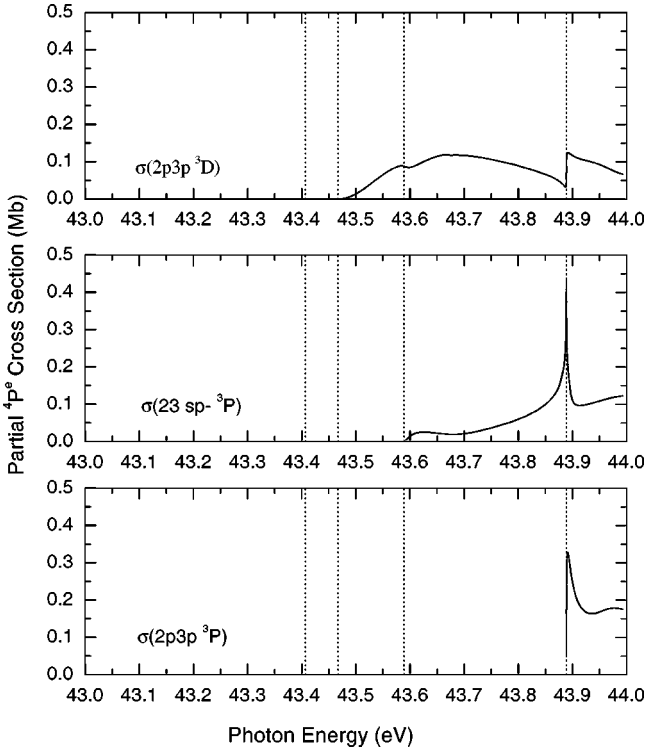

FIG. 6. Partial $^4P^e$ photodetachment cross sections leading to $2p3p\ ^3D$, $23sp-\ ^3P$, and $2p3p\ ^3P$ states of neutral He. The vertical dashed lines represent the He $23sp+^3P$, $2p3p\ ^3D$, $23sp-\ ^3P$, and $2p3p\ ^3P$ thresholds, respectively.

The vertical dashed lines indicate the thresholds $23sp+\ ^3P$, $2p3p\ ^3D$, $23sp-\ ^3P$, and $2p3p\ ^3P$, respectively.

A resonance, just below the $23sp+\ ^3P$ threshold, located at 43.37 eV with a width of 14.4 meV, is seen. This resonance is strongly mixed and is designated as $(2s3p^2+2p3s3p)\ ^4P^e$ or $((2s3p+3s2p)\ ^3P)3p\ ^4P^e$. This resonance decays almost exclusively to the $2p^2\ ^3P$ and $2s2p\ ^3P$ channels, seen in Fig. 5. Decay to the various $1snl$ channels is very small (less than 2% of the total) due to the fact that the $1s$ wave function is so compact compared to the $n=2$ orbitals. For this resonance, seen also in Fig. 2, the position, height, and shape are in good agreement with Ref. [13]. But we find none of the structures between the $2p^2\ ^3P$ threshold at 39.98 eV and this resonance, which are found in Ref. [13].

Above the $23sp+\ ^3P$ threshold at 43.41 eV, the rise from the threshold characteristic of photodetachment is seen in $\sigma(23sp+\ ^3P)$ in Fig. 5. It is evident that $\sigma(2p^2\ ^3P)$ and $\sigma(2s2p\ ^3P)$ are also substantial in this region. In other words, detachment *plus* excitation constitutes the major portion of the total $^4P^e$ cross section in this range. In addition, the $1snl$ triplet channels are not shown because they contribute a maximum of only about 2% to the total $^4P^e$ cross section in this energy region.

Going up further in energy, the situation is shown in Fig. 5 along with Fig. 6. The rise from each new threshold is seen. Furthermore, the effect of interchannel coupling is clearly evident with the opening of each new channel. Where the new channel opening is not very strong, as in the case of $\sigma(2p3p\ ^3D)$ and $\sigma(23sp-\ ^3P)$ seen in Fig. 6, the inter-

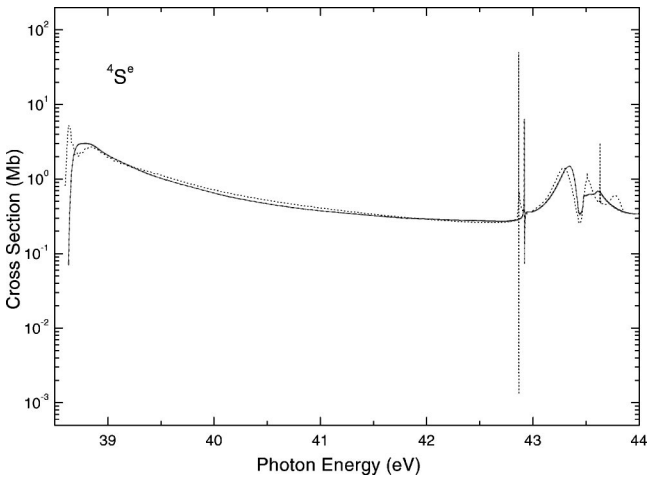

FIG. 7. $^4S^e$ photodetachment cross section of the $1s2s2p\ ^4P^o$ state of He^- from the $1s$ threshold to 44 eV. Present results: solid line, length form; dashed line, velocity form (results in length from and in velocity form are superimposed); the dotted line shows the result of Ref. [13].

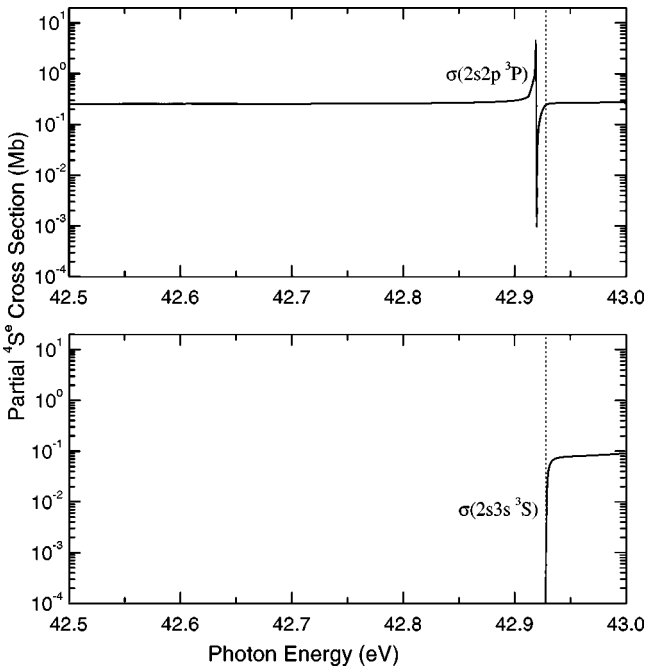

FIG. 8. Partial $^4S^e$ photodetachment cross sections leading to $2s2p\ ^3P$ and $2s3s\ ^3S$ states of neutral He. The vertical dashed line represents the He $2s3s\ ^3S$ threshold.

channel coupling effects of the newly opened channel on the cross sections of the other open channels is correspondingly small. But, at the opening of the $2p3p\ ^3P$ channel (Fig. 6) which has a large cross-section peak just above its threshold, there are significant structures seen in each of the other open channels shown in Figs. 5 and 6. These are very likely manifestations of a resonance just below (and overlapping) the $2p3p\ ^3P$ threshold, possibly a $2s3p4s\ ^4P^e$ resonance. This type of behavior has been found previously for outer-shell photodetachment both theoretically [6,7] and experimentally [21].

Finally, in connection with the $^4P^e$ cross sections, it is quite evident from Figs. 5 and 6 that photodetachment plus excitation dominates at the highest energies shown. The total $^4P^e$ photodetachment cross section at 44 eV is seen, from Fig. 2, to be slightly above 0.8 Mb; within the $^4P^e$ manifold, photodetachment cross section with the other electrons remaining unchanged, $(2s2p\ ^3P)$, is seen in Fig. 5 to be about 0.15 Mb, or less than 20% of the total. Thus, at 44 eV, $1s$ photodetachment plus excitation is more than 80% of the total $1s$ photodetachment cross section in the $^4P^e$ manifold.

B. $^4S^e$ photodetachment cross section above the $1s$ threshold

The cross section to the final $^4S^e$ state is shown in Fig. 7; the first peak of the cross section is the result of the $1s2s2p\ ^4P^o \rightarrow (2s2p\ ^3P)kp\ ^4S^e$ channel. As in the $^4P^e$ case discussed in the preceding section, this is not a resonance but threshold behavior. Only one inner-shell $^4S^e$ channel is open here and there is only the one peak near threshold. The results of Ref. [13], also shown in Fig. 7, exhibit a double-peak structure in the threshold region, a behavior that differs from the present results and that we do not understand. Our calculation shows a very narrow $2s3s4s\ ^4S$ resonance at 42.919 eV, width 0.12 meV about 9 meV below the $2s3s\ ^3S$ threshold. Using a very fine energy grid, we find the peak cross section to be 6.72 Mb in the length formulation (6.10 Mb in velocity). This is seen to be in general agreement with Ref. [13]. Above this narrow resonance, the next peak, due to the nonresonant transition to the $(2s3s\ ^3S)ks$ state, is located at 43.35 eV, in quite good agreement with Ref. [13]. But above this peak, our calculations show significant difference from Ref. [13], as seen from Fig. 7, just as was seen in the $^4P^e$ case above.

The individual channel cross sections are shown in detail in Figs. 8–10. The detailed Fano profile of the $2s3s4s$ resonance in the $2s2p\ ^3P$ cross section (Fig. 8) is quite evident. In addition, the peak at 43.35 eV, in the $2s3s\ ^3S$ cross section (Fig. 9) is seen to lie about 0.42 eV above the $2s3s\ ^3S$ threshold; this peak results from the $1s2s2p\ ^4P^o \rightarrow (2s3s\ ^3S)ks\ ^4S^e$ transition. Since it is a $p \rightarrow s$ transition, this cannot be a delayed maximum due to an angular momentum barrier. Further, the eigenphase sum shows only smooth behavior in the region of this peak; thus it is not due to a resonance. In any case, it is much wider (by more than an order of magnitude) than the typical negative-ion resonance. To uncover the origin of this peak, MCHF calculations of the photodetachment [11,12] of this channel were performed. These give results similar to what is shown in Fig. 9, and permit a detailed study of the contributions to the dipole matrix element. Since the agreement between *R*-matrix and single-channel MCHF results is rather good, interchannel effects are not the cause of this peak. Also this is the largest cross section by far at the maximum and small cross sections do not significantly alter large ones. Since the initial $1s2s2p\ ^4P^o$ state of He^- is strongly mixed with $1s2s3p\ ^4P^o$ (coefficients 0.86 and 0.45, respectively) and the final $2s3s\ ^3S$ state of He is strongly mixed with $2p3p\ ^3S$ (coefficients 0.81 and 0.59, respectively), the dipole ma-

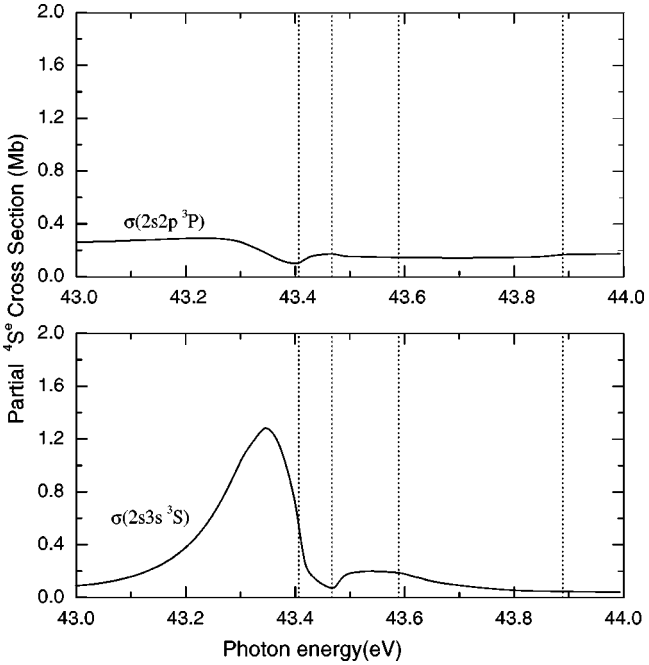

FIG. 9. Partial $^4S^e$ photodetachment cross sections leading to $2s2p\ ^3P$ and $2s3s\ ^3S$ states of neutral He. The vertical dashed lines represent the He $23sp+\ ^3P$, $2p3p\ ^3D$, $23sp-\ ^3P$, and $2p3p\ ^3P$ thresholds, respectively.

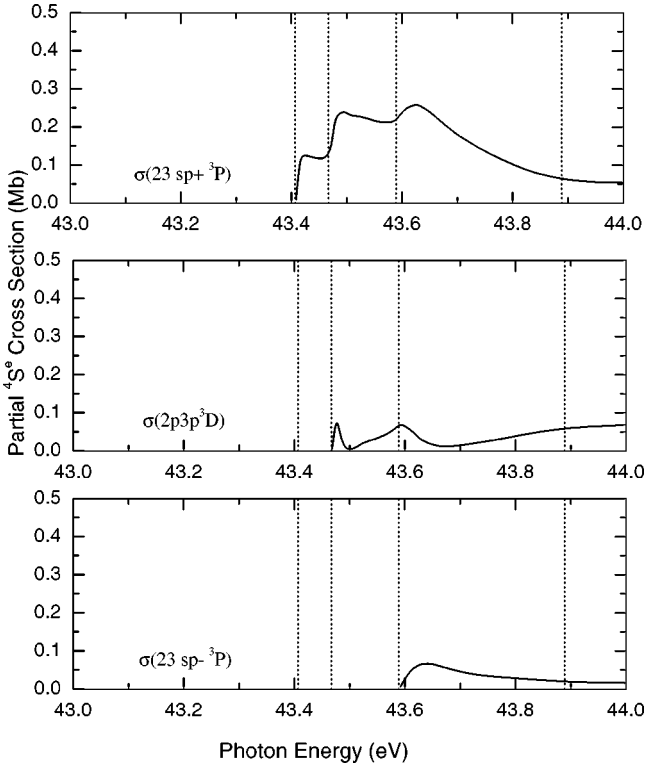

FIG. 10. Partial $^4S^e$ photodetachment cross sections leading to $23sp+\ ^3P$, $2p3p\ ^3D$, and $23sp-\ ^3P$ states of neutral He. The vertical dashed lines represent the He $23sp+\ ^3P$, $2p3p\ ^3D$, $23sp-\ ^3P$, and $2p3p\ ^3P$ thresholds, respectively.

trix element is quite complicated. Various cancellations thus suppress the cross section very near threshold, but increasing it a little above threshold leads to the situation seen.

In a general sense then, this behavior is caused by a complicated multiconfiguration overlap effect, much as a Cooper minimum results from a single-configuration overlap effect. These multiconfiguration effects must occur in atoms as well, but there they are likely to be small and difficult to pick out. But in negative ions, where correlation effects dominate the dynamics, multiconfiguration effects of the type seen here are most likely quite common.

At the higher energies, seen in Figs. 9 and 10, the cross sections exhibit a variety of complicated behaviors. These behaviors are nonresonant and occur due to interchannel coupling effects, multiconfiguration effects (as described above), and the fact that photodetachment cross sections rise from zero at threshold, giving the appearance of resonances. The largest of the higher-energy cross sections is the $23sp\ +\ ^3P$ channel which has a rather peculiar shape, induced primarily by the multiconfiguration overlap effect along with interchannel coupling with the $2s3s\ ^3S$ and $2s2p\ ^3P$ channels. In addition, the $2p3p\ ^3D$ channel shows particularly interesting structure, induced mostly by interchannel coupling with the stronger channels, including induced Cooper minima at 43.50 and 43.67 eV. At the highest energies, photodetachment plus excitation represents about half of the total $^4S^e$ cross section as opposed to the $^4P^e$ even case where two-electron processes accounted for 80% of the total. Finally, we reiterate that between 43.5 and 44 eV the present results differ even qualitatively from Ref. [13].

C. $^4D^e$ photodetachment cross section above 1*s* threshold

Figure 11 shows the photodetachment cross section to the final $^4D^e$ state. The first peak results from the $2s2pkp\ ^4D^e$ channel, which increases rapidly from threshold to a maximum of about 22 Mb. Our results differ dramatically from those of Ref. [13], also shown in Fig. 11: they report three

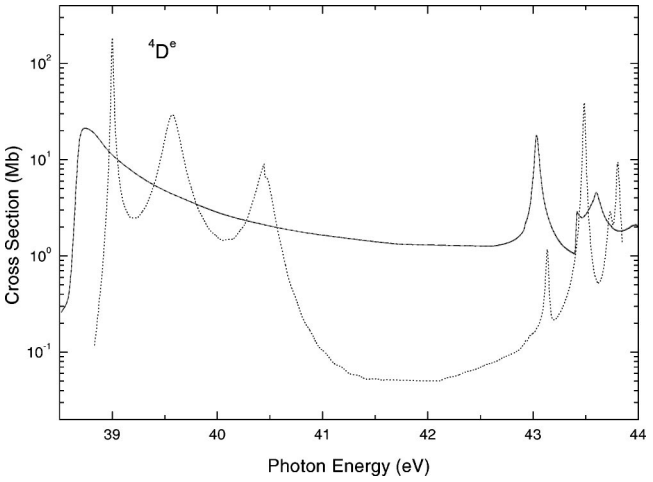

FIG. 11. $^4D^e$ photodetachment cross section of the $1s2s2p\ ^4P^o$ state of He^- from the 1*s* threshold to 44 eV. Present results: solid line, length form; dashed line, velocity form (results in length from and in velocity form are superimposed); the dotted line shows the result of Ref. [13].

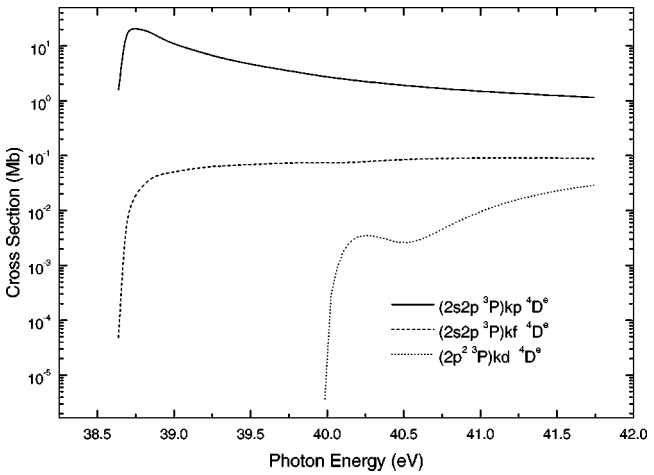

FIG. 12. Partial $^4D^e$ photodetachment cross section to $(2s2p\ ^3P)kp\ ^4D^e$, solid line; $(2s2p\ ^3P)kf\ ^4D^e$, dashed line; and $(2p^2\ ^3P)kd\ ^4D^e$, dotted line.

peaks arising from $2s2pkp$, $2s2pkf$, and $2p^2kd\ ^4D$ channels, respectively. In order to investigate this in detail, in Fig. 12 the partial cross sections for each channel are shown. Here it is seen that the partial cross section for the $2s2pkf\ ^4D^e$ channel is about two orders magnitude smaller than $2s2pkp\ ^4D^e$ channel. From a mathematical point of view, this is because there exists a one-electron transition from the initial state $1s2s2p\ ^4P^o$ to the $2s2pkp\ ^4D^e$ final state, but the $2s2pkf\ ^4D^e$ final state can only be reached via correlation. Therefore the contribution of $2s2pkf\ ^4D^e$ is small. As for $2p^2kd\ ^4D^e$ the cross section is even smaller, three orders of magnitude smaller than that of $1s2s2p\ ^4D^e$ for similar reason. In addition, further above threshold, we see from Fig. 11 rather dramatic differences, by more than an order magnitude, of the background $^4D^e$ detachment cross section between our results and Ref. [13]. This is surprising since the background cross sections were found in quite good agreement for transition to ^4P and ^4S final states. Furthermore, the present results are in quite good agreement in this region with the earlier MCHF results [11,12]. We cannot explain this discrepancy. Between 43 and 44 eV some structure in the $^4D^e$ cross section is found, as seen in Fig. 11. To understand the details here, $^4D^e$ cross sections leading to the various state of He are shown in Figs. 13–15. From Fig. 13 the opening of the $2s3s\ ^3S$ channel is clearly seen. The cross section for this two-electron detachment plus excitation channel reaches a huge maximum of about 12 Mb. This is a nonresonant transition, $1s2s2p\ ^4P^o \rightarrow (2s3s\ ^3S)kd\ ^4D^e$, starting from zero at threshold because it is a photodetachment, and having its maximum several tenths of an eV above threshold owing to the *d*-wave angular momentum barrier. In addition, significant effects of interchannel coupling are seen, particularly with the $2s2p\ ^3P$ cross section, within the $^4D^e$ manifold. The total $^4D^e$ photodetachment is then about 20 Mb, at this maximum, as seen in Fig. 11. We reiterate, however, that this peak just above 43 eV is not a resonance. Note that this feature was also seen by Ref. [13] at just about the same energy, but with a markedly reduced cross section, as shown in Fig. 11.

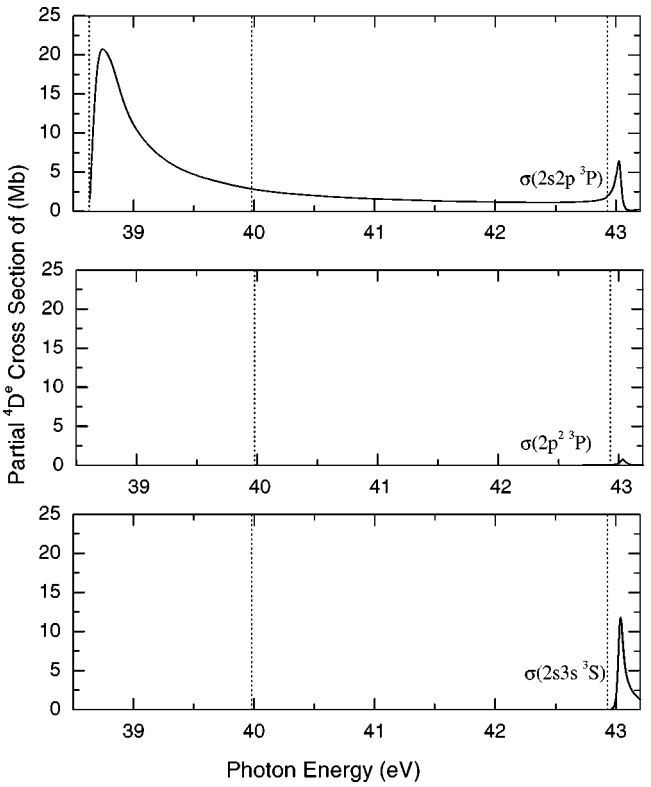

FIG. 13. Partial $^4D^e$ photodetachment cross sections leading to $2s2p\ ^3P$, $2p^2\ ^3P$, and $2s3s\ ^3S$ states of neutral He. The vertical dashed lines represent the He $2p^2\ ^3P$ and $2s3s\ ^3S$ thresholds, respectively.

Going further up in energy the present results are seen to be completely different from those of Ref. [13]. At the next threshold, $23sp+\ ^3P$, a significant rise from threshold is seen in the newly opened channel, along with interchannel effects in each of the other open channels, shown in Fig. 14.

Again, as in the $^4S^e$ case, several of the higher-energy cross sections exhibit complex behavior as a function of energy. And, as in the $^4S^e$ case, these behaviors are due to a combination of interchannel coupling, multiconfiguration overlap effects, and the rises from the zero cross section at the opening of each new channel. Similar to the $^4P^e$ case, at the highest energies, the contribution of detachment plus excitation is seen to be about 80% of the total $^4D^e$ cross section.

D. Total photodetachment cross section above 1*s* threshold

The total photodetachment cross section for $1s2s2p\ ^4P^o$, the sum of $^4S^o$, $^4P^o$, and $^4D^e$ cross sections, is shown in Fig. 16 from the 1*s* threshold to 44 eV; for comparison the results of Ref. [13] are also shown. The differences noted in the partial cross sections are, of course, reflected here as well. It is noteworthy that the first maximum in the cross section, with a peak value of about 30 Mb, is in excellent agreement with the MCHF result [11,12]. This agreement is expected since the MCHF calculation omitted interchannel coupling, which, as seen in the preceding discussion, should not be important here. This gives us some confidence in the

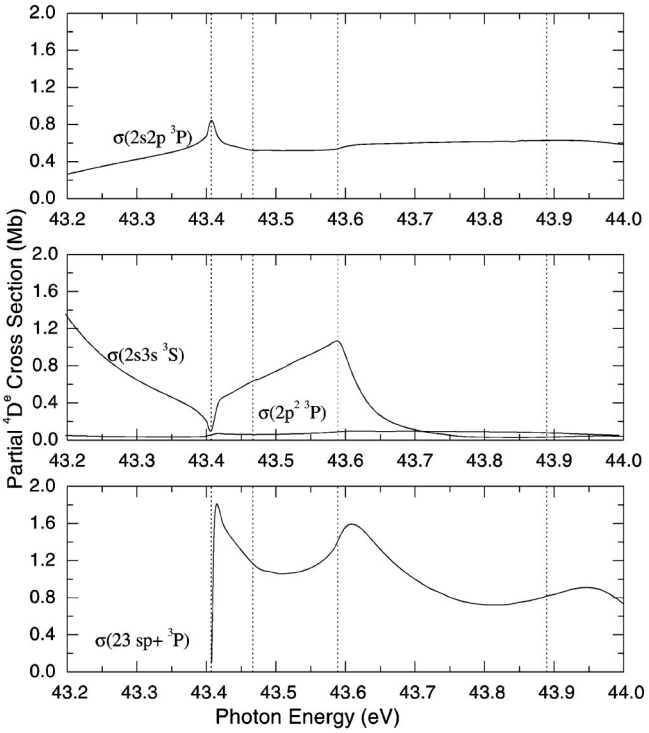

FIG. 14. Partial $^4D^e$ photodetachment cross sections leading to $2s2p\ ^3P$, $2p^2\ ^3P$, $2s3s\ ^3S$, and $23sp+\ ^3P$ states of neutral He. The vertical dashed lines represent the He $23sp+\ ^3P$, $2p3p\ ^3D$, $23sp-\ ^3P$, and $2p3p\ ^3P$ thresholds, respectively.

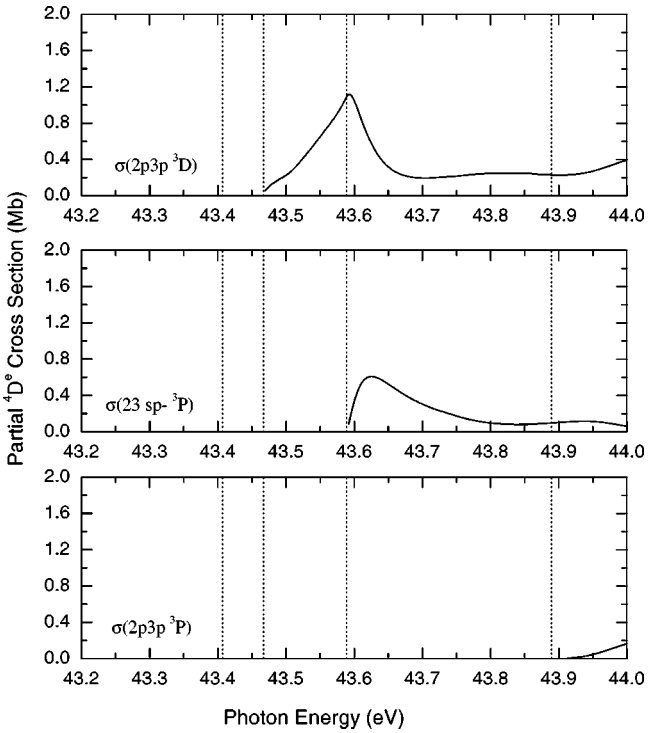

FIG. 15. Partial $^4D^e$ photodetachment cross sections leading to $2p3p\ ^3D$, $23sp-\ ^3P$, and $2p3p\ ^3P$ states of neutral He. The vertical dashed lines represent the He $23sp+^3P$, $2p3p\ ^3D$, $23sp-^3P$ and $2p3p\ ^3P$ thresholds, respectively.

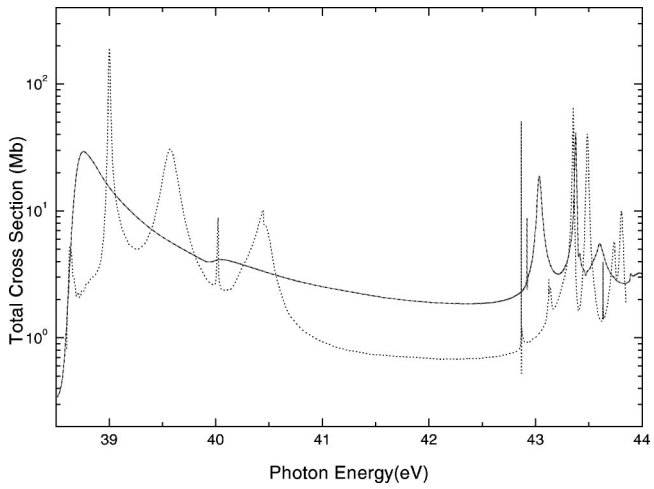

FIG. 16. Total photodetachment cross section of He^- $(1s2s2p\ ^4P^o)$ from the $1s$ threshold to 44 eV. The solid and dashed lines are the resent results in length and velocity formulations (they are superimpposed), and the dotted curved is from Ref. [13].

results of the present calculation. But we still have no clue as to the disagreement between the present results and Ref. [13], a disagreement which is so evident in Fig. 16.

The total cross section includes transition to the $1snl$ final states of He, as well as the doubly excited states, but for reasons discussed in connection with the $^4P^e$ final channels, the sum of the transitions leaving He in the $1snl$ final states is negligible, less than 2% of the total. In addition, starting at 43 eV, just above the opening of the first detachment plus excitation channel, where the He is left in the $2s3s\ ^3S$ state, two-electron detachment plus excitation processes dominate the total cross section. By the highest energy considered, 44 eV, single-electron detachment of the $1s$ leading to the $2s2p\ ^3P$ state of He is only about 20% of the total.

IV. CONCLUDING REMARKS

Using the *R*-matrix methology which was modified to deal with asymptotic boundary conditions appropriate to photoabsorption by negative ions, the photodetachment of the $1s2s2p\ ^4P^o$ state of He^- has been investigated in the energy region around the $1s$ detachment threshold. The structure of the $1s$ photodetachment cross section differs dramatically from the $1s$ photoionization cross sections of neutral atoms or positive ions; this occurs despite the fact that the $1s$ wave function in He^- is almost exactly the same as in He^+, owing to the location of the bulk of the $2s$ and $2p$ charge density at quite large values of r. It is therefore the final continuum state that causes the dramatic difference in the two cases; for He^+, the final state is a pure $Z=2$ Coulomb wave function, while for He^-, the final-state wave function is quite complicated and ''sees'' a neutral atom asymptotically.

The asymptotic form of the final-state (continuum) wave function plays a crucial role at detachment thresholds. For photoionization of atoms and positive ions, where the photoelectron leaves a positively charged photoion behind, the

TABLE V. Positions (photon energy) and widths for resonances found in $He^-\ 1s2s2p$ photodetachment in the region of the $1s$ threshold.

	Present work		Other calculations	
States	E_r (eV)	γ (mev)	E_r (eV)	γ (mev)
$2s2p^2\ ^4P^e$	37.703	9.736	37.669 [a]	9.850 [a]
			37.683 [b]	9.22 [b]
$2s3p^2+2p3s3p\ ^4P^e$	43.370	14.40	43.353 [a]	12.607 [a]
$2s3p4s\ ^4P^e$	43.888	8.50		
$2s3s4s\ ^4S^e$	42.919	0.12	42.866 [a]	0.103 [a]

[a]Reference [13].
[b]Reference [12].

threshold cross section is finite. In the case of photodetachment, where the photoelectron interacts with a residual neutral atom, there is no solution at zero photoelectron energy other than the trivial; therefore the threshold photodetachment cross-section vanishes. This rise of each partial cross section from zero at each detachment threshold contributes to the complexity of the inner-shell photodetachment cross section.

Resonances are also found but far fewer than in photoionization of neutral atoms and positive ions; negative ions do not support Rydberg series. In fact no resonances at all were found below most of the thresholds. A huge $2s2p^2\ ^4P^e$ resonance appears just below the first $1s$ detachment threshold, a $(2s3p^2+2p3s3p)\ ^4P^e$, a $2s3s4s\ ^4S^e$, and possibly a $2p3p4s\ ^4P^e$ were also pinpointed. No other $1s$ excitation resonances emerged in the present study up to a photon energy of 44 eV. These resonance positions and widths are shown in Table V.

Throughout the energy range considered, correlation in form of interchannel coupling was found to be of crucial importance, particularly in the vicinity of detachment thresholds. This is a generalization of the phenomenon in photoionization of atoms and positive ions where interchannel coupling affects outer-shell thresholds [22]. In addition, a phenomenon was found, the multiconfiguration overlap effect, which is a multiconfiguration analog of the type of single-configuration overlap effect that produces a Cooper minimum. The combined action of all of these phenomena produces the complexity seen in the cross section of this highly correlated system.

The strength of the correlation is also evident in the two-electron detachment plus excitation process. In atoms, these two-electron processes associated with inner-shell photoionization typically amount to $\sim$10% of the total photoabsorption. For $1s$ photodetachment from the $He^-\ 1s2s2p\ ^4P^o$ initial state this two-electron process was found to *dominate* the total photoabsorption cross section wherever they are energetically possible.

The comparison with a previous theoretical result [13] showed major discrepancies, even though the calculation of Ref. [13] in principle included the same correlation effects that are included in the present calculations. While there are certainly regions of good agreement, significant differences in many structures were demonstrated. Furthermore, in the broad structureless 41–43 eV region in the $^4D^e$ cross section, the calculations differ by an order of magnitude. In the absence of dynamical effects, the $^4S^e$, $^4P^e$, and $^4D^e$ cross sections will be in a ratio of 1:3:5. The present results were seen to be roughly in that proportion. The results of Ref. [13] are not; the $^4D^e$ cross section is an order of magnitude too small in this region. This suggests (but certainly does not prove) that the present results are more accurate than those of Ref. [13]. Experimental investigation of the photodetachment of the metastable $1s2s2p\ ^4P^e$ state of He^- is urgently needed to sort out the situation.

ACKNOWLEDGMENTS

We are grateful to Jinhua Xi and Charlotte Froese Fischer for providing us with the numerical data from their calculation, and Nigel Badnell for allowing us to use his perturbative asymptotic code and to compare with our codes. The use of computing facilities at the Center for Theoretical Studies of Physical System, Clark-Atlanta University, is gratefully acknowledged. This work was supported by NSF, NASA, and IDRIS (France).

[1] S.J. Buchman and C.W. Clark, Rev. Mod. Phys. **66**, 539 (1994), and references therein.
[2] K.A. Berrington, W.H. Eissner, and P.H. Norrington, Comput. Phys. Commun. **92**, 290 (1995).
[3] K. L. Bell, K. A. Berrington, and C. A. Ramsbottom, in *Atomic and Molecular Physics*, edited by I. Alvarez, C. Cisneros, and T. J. Morgan (World Scientific, Singapore, 1994), pp. 176–186, and references therein.
[4] C.A. Ramsbottom and K.L. Bell, J. Phys. B **32**, 1315 (1999).
[5] M. Le Dourneuf and L. Vo Ky, J. Phys. B **10**, L35 (1977).
[6] C.N. Liu and A.F. Starace, Phys. Rev. A **60**, 4647 (1999).
[7] J. Xi and C. Froese Fischer, Phys. Rev. A **53**, 3169 (1996).
[8] C.W. Walter, J.A. Seifert, and J.R. Peterson, Phys. Rev. A **50**, 2257 (1994).
[9] J.P. Croskery, N.S. Scott, K.L. Bell, and K.A. Berrington, Comput. Phys. Commun. **27**, 385 (1982).

[10] M. Gailitis, J. Phys. B **9**, 843 (1976).
[11] D.S. Kim, H.L. Zhou, and S.T. Manson, Phys. Rev. A **55**, 414 (1997).
[12] D.S. Kim, H.L. Zhou, and S.T. Manson, J. Phys. B **30**, L1 (1997).
[13] J. Xi and C. Froese Fischer, Phys. Rev. A **59**, 307 (1999).
[14] L. Vo Ky, P. Faucher, A. Hibbert, J.-M. Li, Y.-Z. Qu, J. Yan, J.C. Chang, and F. Bely-Dubau, Phys. Rev. A **57**, 1045 (1998).
[15] A. Hibbert, Comput. Phys. Commun. **9**, 141 (1975).
[16] J.F. Perkins, Phys. Rev. **178**, 89 (1969).
[17] B. Schiff, C.L. Pekeris, and Y. Accad, Phys. Rev. A **4**, 885 (1971).
[18] J.A. Fernley, K.T. Taylor, and M.J. Seaton, J. Phys. B **20**, 6457 (1987).
[19] L.C. Green, N.C. Johnson, and E.K. Kolchin, Astrophys. J. **144**, 369 (1996).
[20] P. Kristensen, U.V. Pedersen, V.V. Petrunin, T. Andersen, and K.T. Chung, Phys. Rev. A **55**, 978 (1997), and references therein.
[21] J. Dellwo, Y. Liu, D.J. Pegg, and G.D. Alton, Phys. Rev. A **45**, 1544 (1992).
[22] M. Ya. Amusia, *Atomic Photoeffect* (Plenum Press, New York, 1990) and references therein.